Development and characterisation of novel anti-bacterial S-phase based coatings

Formosa, Dennis; Li, Xiaoying; Dong, Hanshan; Sammons, Rachel

DOI:
10.1016/j.tsf.2017.10.054

Development and Characterisation of Novel Anti-Bacterial S-Phase Based Coatings

Dennis Formosa[1], Xiaoying Li[1*], Rachel Sammons[2] and Hanshan Dong[1]

[1] School of Metallurgy and Materials, University of Birmingham, Birmingham B15 2TT, UK
[2] School of Dentistry, University of Birmingham, Birmingham B15 2TT, UK

Abstract:

It is well-known that biologically active Ag/Cu ions are strong bactericides and silver or copper nanoparticles have been used in polymer-based antibacterial coatings. However, their poor durability has limited their use in tribological applications. This problem has been largely addressed recently by developing novel plasma co-alloying of austenitic stainless steel surfaces with both nitrogen and Ag/Cu to form wear resistant antibacterial S-phase. However, this technology is only applicable to austenitic stainless steel as the S-phase cannot be formed to other materials.

In this study, S-phase based anti-bacterial coatings have been, for the first time, developed using magnetron sputtering through co-deposition of austenitic stainless steel with Ag/Cu to form hard S-phase doped with Ag, Cu or both in monolayer and multilayer structures. These coatings were fully characterised using multiple techniques such as SEM, TEM, XRD, GDOES and anti-bacterial tests. It has been found that it is possible to produce dense Ag and Cu doped S-phase layer with significant anti-bacterial efficacy. This was achieved while preserving the advantageous properties of the S-phase microstructure. As opposed to the popular diffusion based S-phase production such as plasma nitriding, this technology can also be applied on all kinds of surfaces, including low-cost steel surfaces, polymers and ceramics.

* Corresponding author

1. Introduction

Hospital Acquired Infections (HAI) increase the mortality rate and cause an increased demand for intensive care units, extended post-operation hospital stays and additional surgical intervention [1]. Nosocomial infections claim the life of 80,000 people annually in the United States of America (USA) making it the eighth highest cause of loss of life in the USA [2]. This also brings about a cost of more than $5 billion annually [2]. In the European Union Surgical Site Infections (SSI) are among the most common form of HAIs [3].

Medical devices such as surgical implants have brought about improvement in the quality of life of those who require them. However, the hospital stay and implantation of such devices can cause the proliferation of bacteria such as gram-positive S*taphylococcus aureus*. This occurs due to bacterial adhesion to equipment utilised during surgical intervention such as scalpels, scissors and the surgical implants themselves [4]. Other surfaces found within the hospital such as door knobs, bed side tables can also harbour infectious organisms which often spread quickly through people's hands [5]. Prophylactic measures through antibiotic administration or implementation of strict hygiene procedures are known to reduce or limit the negative impact of such bacteria but not prevent it completely [4, 6]. Around 5% of primary Total Hip Joint Replacement (THJR) surgical sites become infected while there is a probability of 15%-20% that the revision surgery is also infected [4, 6]. Complex infections often require revision surgery as antibiotic treatment is often unable to control the localised infection [6]. Over-reliance on antibiotics causes high predominance of outbreaks of antibiotic resistant bacteria such as *Methicillin-resistant Staphylococcus aureus* which are not unheard of in hospitals [7].

Implantable devices including bone plates, external fixation devices, nails and screws are often manufactured from austenitic stainless steel (AISI 316L alloy) owing to its attractive properties (cost, good corrosion resistance and biocompatibility) [8]. Such an alloy however

suffers from significant pitting and crevice *in vivo* corrosion, excessive wear (including fretting wear), local bacterial infection or a combination of such failure causes [8-13]. Such surface phenomena produce metallic debris in the immediate area while causing excessively high levels of dissolved metal ions (such as nickel which is a known allergen [14] and carcinogen [15]) in the body fluids and organs causing serious medical complications [15, 16].

High performing surgical grade metals such as titanium and cobalt-chromium are available; however they cost up to ten times more than austenitic stainless steel [15]. Alternatively, one can surface engineer austenitic stainless steel in order to enhance the surface mechanical properties such as corrosion and wear resistance. It has been proven that austenitic stainless steel can be surface engineered through a low temperature thermo-chemical surface diffusion treatment (temperature <430°C in a nitrogen containing atmosphere) [13]. Such treatments create an *S-phase* layer at the surface which exhibits significantly improved mechanical properties. However, it is known that S-phase can be formed only on some specific metallic materials including austenitic stainless steel, Co-Cr alloys and Ni-Cr alloys [13].

S-phase surfaces can be also be produced through magnetron sputtering techniques where austenitic stainless steel is deposited onto substrates within a nitrogen containing atmosphere [17]. Such surfaces have shown to exhibit all the superior properties of diffusion S-phase layers albeit in a narrower layer (2μm) [18-20]. Magnetron sputtering introduces advantageous flexibilities where one can co-deposit S-phase together with other alloying elements not traditionally associated with S-phase. The introduction of such elements is a feasible way to elicit novel properties within S-phase coatings albeit no reports of such studies are available at the time of writing. S-phase diffusion layers on the other hand have been previously alloyed with silver or copper [21, 22]. Silver and copper have received significant attention in surface research targeting the medical industry owning to their high efficiency with which they eliminate bacteria [23, 24]. The aim of this study was to investigate and report for the

first time the microstructural characteristics and anti-bacterial efficacy of S-phase coatings containing silver or copper in various monolayer and multilayer architectures.

2. Experimental details

2.1 Substrate materials

Annealed industrial grade AISI 316 (having a composition (wt%) of 17% Cr, 10.2% Ni, 2.5% Mo, 2% Mn, 1% Si, 0.08% C, 0.045% P, 0.03% S and Fe balance) was utilised during the preparation of the specimens. These specimens were prepared from a 14mm round bar (cut at 1.2mm thicknesses for anti-bacterial studies, supplier: RS components UK) and a 25.4mm round bar (cut at 6.2mm thicknesses for other characterization analysis, supplier: RS components UK). All specimens were progressively ground to a finish level of 1200 grit size using SiC sand paper after which they were polished to a mirror finish using diamond suspension paste (1μm). Specimens were thoroughly cleaned in warm acetone before loading in the deposition machine.

2.2 Coating deposition

2.2.1 Machinery Setup

The coatings presented in this study were produced using a Closed Field Unbalanced Magnetron Sputtering Ion Plating Machine (CFUMSIP) UDP-350/4 which was manufactured by Teer Coatings Ltd. (UK). A plan view of the setup used to deposit the monolayer coatings in this study is presented in Figure 1. Two AISI316L stainless steel targets with a chemical composition (wt%) of 16.6% Cr, 11.02% Ni, 2.02% Mo, 1.26% Mn, 0.43% Si, 0.024% C, 0.04%N, 0.032% P, 0.002% S with an Fe balance were utilised in this study. One chromium target (99.5% purity) was utilised for all coatings and a silver (99.95% purity) or copper (99.5% purity) was utilised in order to produce alloyed S-phase coatings.

2.2.1 Deposition Procedure

Prior to coating production, the sputtering machine and targets were ion cleaned using a reproducible pre-programmed argon gas only run in order to avoid target nitrogen 'poisoning'. Coating deposition was started only after a base pressure of 10^{-6} Torr was attained with a vacuum diffusion pump so to minimize contamination. Testo temperature sensitive labels were used in order to confirm the maximum temperature during deposition. A piece of polished silicon wafer was loaded alongside the AISI 316 specimen in order to facilitate fracture analysis.

The basic parameters utilised to deposit all the coatings in this study were as follows: 900s of pre-treatment ion cleaning using a bias voltage of -400V and argon only plasma, 310s of chromium interface layer deposition with a target current of 1A and a specimen pulsed bias voltage of -60V (having a frequency of 250Hz and a pulse width of 500nsec), deposition of S-phase mono/multilayer with a AISI 316L target current of 1.5A and a specimen pulsed bias voltage of -60V (having a frequency of 250Hz and a pulse width of 500nsec) and a nitrogen flow rate of 8sccm. Additions of silver or copper were performed during this step as described in the subsequent sections. Argon flow is 8sccm throughout all the recipe. Such parameters were chosen after a parameter optimization study. The coated specimens were allowed to cool down under vacuum before extraction from deposition chamber. The maximum deposition temperature during the treatment was found to be less then 204°C.

2.2.1.1 Monolayer coatings

The homogeneous monolayer coatings were performed by simply powering the target of the antibacterial agent and the AISI316L simultaneously during the S-phase deposition step. The deposition time of this step was varied in order to produce an overall coating thickness of 2µm. Three coatings for each antibacterial agent were performed using the following target current settings during the S-phase deposition step only and coating designation: silver 0.2A (SAglow), 0.35A (SAgmid), 0.5A (SAghi) and copper 0.32A (SCulow), 0.43A (SCumid), 0.54A (SCuhi). A high silver concentration S-phase monolayer coating was produced using similar techniques

for microscopic analysis. All specimens were mounted on a jig with a target to specimen distance of between 63mm to 73mm and the specimen holder rotation was set to 5rpm.

2.2.1.2 Multilayer coatings

These coatings consist of layers of equal thicknesses alternating between pure S-phase and silver/copper. The setup utilised for multilayer coatings was similar to that of Figure 1 however only one AISI 316L target was employed which was mounted opposite that silver/copper target in order to form sharp interfaces between the layers. The target current settings utilised were 0.36A for silver and 0.51A for copper. Three coatings for each antibacterial agent with varying layer thicknesses were performed after depositing the chromium interface layer using the following layer thicknesses (thickness was controlled through specimen holder revolution speed): silver 2.5nm (SAg2.5), 10nm (SAg10), 35nm (SAg35) and copper 2.5nm (SCu2.5), 10nm (SCu10), 35nm (SCu35). Specimen holder rotation was set to 6.5rpm, 1.5rpm and 0.5rpm in order to produce the 2.5nm, 10nm and 35nm multilayer coatings respectively. Owning to the nature of copper and affinity to nitrogen the copper layers were deposited in an atmosphere that contained only argon while silver containing multilayers were deposited in argon and nitrogen containing atmosphere. A barrel-type sample holder with target to specimen distance of 73mm was used for depositing multilayer coatings. A silver or copper layer was deposited as the final top layer with the respective thickness.

2.3 Microstructure characterisation

A JOEL 7000F (Japan) Scanning Electron Microscope (SEM) equipped with a calibrated Oxford Instrument (UK) Wave Dispersive Spectroscopy (WDS) detector was utilised and chemical composition analysis while the secondary electron detector was used for microscopic imaging of coating surfaces and fracture cross-sections. The SEM was operated at 20kV and a 10mm

working distance for imaging and 10kV for WDS investigations. Chemical depth profiling was performed using a Spectruma (Germany) GDA 650HR Glow Discharge Optical Emission Spectroscopy (GDOES) machine using radio frequency mode.

The X-Ray Diffraction (XRD) technique was utilised to help identify the crystalline phases. A Bruker D8 diffractometer equipped with a copper anode ($K_{\alpha 1}$=0.1540nm) with an emission setting of 30kV and 40mA was used to scan the S-phase coated specimens at room temperature conditions. The beam was attenuated using a Germainium crystal and Soller slits (2.5mm at detector, 1mm at source). Using the PANalytical X'Pert HighScore Plus V2.0 software the resulting peaks were identified by comparing them with the International Centre of Diffraction Data (ICDD) database.

Transmission Electron Microscopy (TEM) was performed using a Philips/FEI (US) Technai F20. *In situ* chemical analysis was performed by an Oxford Instruments 80mm^2 X-Max 80 TLE EDS silicone drift detector and the Scanning Transmission Electron Microscopy (STEM) capabilities of the microscope which was configured with a High Angle Annular Dark Field (HAADF) detector. TEM samples were prepared in a cross-sectional fashion by mechanically grinding a slab from the coupon surface followed by further thinning through ion milling of the coating with an FEI (US) Quanta 3D FEG dual beam Focused Ion Beam (FIB) SEM.

2.4 Anti-bacterial efficacy

The anti-bacterial efficacy of the surfaces was analysed using to spread plate method according to standards JIS Z 2801:2000 [25] and BS EN ISO 2196 [26]. A glass cover slip was used as the negative control specimen and a pure copper coupon was used as a positive control specimen. Gram-positive *Staphylococcus aureus* strain NCTC 6571 was utilised owing to its relevance to

HAIs. A single colony of this bacteria was cultured in 10ml of Tryptone Soya Broth (TSB) (Oxoid, UK) and incubated for 12 hours in a shaking incubator at 37 ±1°C. After vortex shaking, the solution was serially diluted four times (using TSB) reducing the bacterial concentration tenfold each time to produce a solution containing approximately 10^5 colony forming units (CFUs) per millilitre. The coated specimens were sterilized using a 70% ethanol solution and dried inside a sterile cabinet. A 90mm sterile petri dish was prepared with a piece of filter paper saturated with 0.9ml of sterile distilled water to increase humidity and a sterile glass slide on top. After placing the sterile specimen onto the glass slide, 50µl of the 10^5 CFU/ml was pipetted onto the coated surface. A 13mm diameter glass cover slip (Thermo Scientific Gerhard Menzel [US]) was gently placed on the droplet to evenly spread out the solution and better control the contact between coating and solution.

The petri dish was then incubated at 21°C for duration times including 60, 90, 120, 360 and 480 min. Afterwards the whole specimen and coverslip assembly was vortex shaken in 10ml of Phosphate Buffer Solution (PBS) (Sigma Aldrich) for 10s in order to dislodge all the viable and non-viable bacteria from the coated surface. The resulting solution was serially diluted twice from which 100µl were spread onto sterile petri dishes prepared with Tryptone Soya Agar (TSA). The spread plates were then incubated overnight at 37°C. The number of colonies (resulting from viable CFUs) formed on the agar represent the number of viable bacteria that survived the contact with coating enabling the classification of the anti-bacterial efficacy through the below equation:

$$Reduction\ (\%) = \frac{\left(N_0 - N_\chi\right)}{N_0} \times 100$$

where N_χ represents the average bacterial concentration at experiment duration 'χ' and N_0 represented the initial bacterial concentration. Three specimens of each coating and control unit were tested and three spread plates were prepared from the three dilutions produced after each test. The results are plotted as average reduction with the respective average error.

3. Results and Discussion

3.1 Cross-sectional microstructure and topography

Figure 2 depicts SEM images of all the silver and copper monolayer coatings produced in this study. The surface morphology of all the monolayer coatings consists of dome-type topped domains with a diameter of around 100nm. However, SAgmid and SAghi exhibit finer domains and irregularly shaped particles on the surface of the coatings respectively. This is potentially related to the higher silver concentration. The lack of surface porosity is apparent across all coatings with varying silver/copper concentrations. Figure 3 shows an image of the fracture surface of coating SCulow resulting after fracturing the silicon wafer substrate. The fracture surface shows high intergranular adhesion and low incidence of porosity due to the weak apparent domain delineation and smooth surface edge. All the other monolayer coatings exhibited similar fracture surfaces.

The images illustrated in Figure 4 show the surface topography of the S-phase/silver and S-phase/copper multilayers under investigation. Figure 5 shows the fracture surfaces of the silver containing multilayers which were similar to those of the copper multilayer coatings. The surfaces of SAg2.5, SCu2.5, SCu10, SCu35 depict loosely packed spherical topped domains which have diameters in the range of 100nm. Some surface porosity can be observed residing between the coating grains. The surfaces of SAg10 and SAg35 on the other hand are characterised by flat platelets and some interdomain porosity. The fracture surface of SAg35 is characterised by delineations at the interfaces between the layers of the coating.

It was noted that the coatings investigated in this study did not exhibit any defects such as blisters, craters or macroparticles which were reported by other researchers [27-29].

3.2 Chemical composition

The surface WDS results for nitrogen, chromium and silver/copper of the monolayer coatings produced in this study are plotted in Figure 6 a, b. As the concentration of silver within the silver containing monolayers increases, the concentration of nitrogen increases initially and then decreases upon further silver additions. The opposite applies for chromium within the same coatings. Copper containing monolayers contained less nitrogen as the copper concentration was increased. Diffusion type S-phase layers typically exhibit a maximum nitrogen concentration of no more than 25at% before nitride phases start to precipitate [13]. The nitrogen concentration exhibited by the S-phase and silver monolayers in this study was higher than those in literature. For instance, SAgmid exhibited a nitrogen concentration of 16.5wt%. Upon taking into consideration the other element this amounts to 50at% of nitrogen concentration, or twice as high than diffusion type S-phase without the formation of nitrides although one XRD peak in Figure 8 (a) remains unconfirmed. Other S-phase coating studies did produce nitrogen concentrations up to 44.44at%; however additional phases were detected through XRD such as γ'-$(Fe, Cr, Ni)_4$ N [30]. Through this study it is possible to conclude that the addition of silver to the S-phase layer allowed such *ultra-saturation* of nitrogen within the S-phase coating as opposed to super-saturation normally reported for S-phase structures. The presence of the larger silver atoms within the lattice enabled new interstitial sites for more nitrogen atoms than basic S-phase only. Copper does not promote such abnormal uptake of nitrogen atoms.

All the multilayer coatings exhibited silver/copper concentrations of around 50wt% which is roughly in line with the equal layer thicknesses for S-phase and silver/copper. Figure 7 shows the chemical depth profile across the whole thickness of multilayer coating SAg35 obtained by the GDOES technique. The fluctuations in the silver concentration highlight clearly the presence of chemically distinct layers. WDS analysis for nitrogen concentration showed that SAg2.5, SAg10 and SAg35 had a nitrogen concentration of 26.3, 22.8 and 18.4wt% respectively.

Figure 14 shows a STEM-EDS map of a cross-section of the SAg10 multilayer coating. It can be observed that the silver layers are deficient in nitrogen when compare to the S-phase layers. Owning to the similar atom plane structure and spacing between S-phase and silver, epitaxial growth was favoured over forming grain boundary defects (see Figure 13). Typically, the (111) S-phase diffraction plane has a d-spacing of around 0.22nm or less [31]. However, all S-phase/silver multilayer coatings in this study exhibit a (111) d-spacing of around 0.24nm (emerging from S-phase and silver, see Figure 10 [a]). Such d-spacing is identical the (111) plane of silver. This shows that owing to the epitaxial growth, the silver layers in this study expand the S-phase lattice beyond the typical expansion, potentially assisting the uptake of interstitial nitrogen. SAg2.5 exhibited the highest nitrogen concentration as well as the strongest (111) peak when compared with the other S-phase/silver multilayers.

As the layer thickness increases the nitrogen content reduces, which is potentially due to the reduced effect of the silver layer as the thickness of the S-phase layer increases.

The copper multilayer SCu2.5, SCu10 and SCu35 on the other hand had a nitrogen concentration of 5.9, 6.3 and 5wt% respectively.

3.3 Phase constituents

3.3.1 X-Ray diffraction

The peaks of austenitic stainless steel lie on the dotted line and are marked as $\gamma(hkl)$ for all diffraction patterns presented in this study. Additionally, the peak associate with the chromium interfacial layer is labelled as Cr - $\alpha(110)$.

Figure 8 a,b show superimposed diffraction patterns of all the silver and copper containing monolayers under study. All six diffraction patterns show strong evidence of S-phase identified by the broad peaks. Labels S(*hkl*) mark all the peaks associated with the S-phase

microstructure. Pure silver exhibits a major peak at a 2θ angle of 44.14° [Ag(200)] as marked on the diffraction pattern. Since this angle coincides with that of Cr - α(110) and S(200) it is difficult to differentiate between phases. All three silver containing monolayers exhibited strong S(200) peaks while the coatings containing 24wt% and 37wt% of silver also exhibit the peak for S(111). The diffraction pattern of the S-phase coating with 24wt% silver concentration also had a strong peak at a 2θ angle of around 38.6°. This peak is potentially emerging from the $Ag_{0.4}Fe_{0.6}$(111). TEM-SAD analysis on a similar coating did not exhibit related diffraction patterns.

All copper containing monolayers exhibit a relatively strong S-phase peak for S(200) and a weaker S(311) peak. Figure 9 graphically shows the lattice parameters of all the monolayers as calculated from the S-phase peaks compared to that of austenitic stainless steel. SAghi exhibits the largest lattice parameter of 0.41nm (emerging from the 200 plane). As the silver concentration within the monolayer reduced, so did the lattice parameter (see Figure 9). All copper monolayers exhibited modest lattice parameter expansions (around 0.397nm).

The diffraction patterns of all the silver and copper multilayer coatings are shown in Figure 10 a,b respectively. All silver multilayer coatings exhibit peaks emerging from the pure silver layer including those for (220), (311), (222) and (111). S-phase peaks are not clearly identifiable however, owing to the fact that both S-phase and silver are face centred cubic in nature and that the layers grow in an epitaxial fashion, and it is possible that S(111) and Ag(111) are superimposed. The copper containing multilayer patterns potentially exhibit similar epitaxial mechanisms to those of silver. Peaks of pure copper coincide with those of the austenitic stainless steel substrate. It is possible that the d-spacing of the S-phase layers are also constrained with that of the copper layers. Coatings SCu10 and SCu2.5 however exhibit a relatively weak peak between γ(111) and γ(200). This peak is potentially associated with the (200) diffraction plane of the S-phase structure.

The S-phase coatings presented in this study exhibit an inherent preferred orientation since only one or two S-phase peaks were detected.

3.3.2 Transmission Electron Microscopy

3.3.2.1 Monolayer

Figure 11 (a) shows a cross sectional bright field image of the S-phase and silver based monolayer containing 42wt% of silver. The diffraction pattern of the selected area in Figure 11 (a) is shown in Figure 11 (b). The bright field image shows that the coating is around 2.4μm thick while the chromium interfacial layer is 130nm thick. Some porosity can be observed to be present within this monolayer as elongated voids between the columnar domains as seen in Figure 11 (a). Some dark particles with a diameter equal of less than 50nm are evident in the bright field image. Point EDS analysis of these particles did confirm that these particles have a relatively high concentration of silver. Figure 11 (b) does show some bright spots on the rings which might potentially be related to the silver particles and therefore having the same lattice parameter as the S-phase.

3.3.2.2 Multilayer

Bright field transmission electron microscopy cross sectional imaging of coating SAg10 is presented in Figure 12 (a, b). The image in Figure 12 (a) shows the whole coating including the chromium interfacial layer while Figure 12 (b) shows s higher resolution image of the initial layers of the coating and the substrate surface. It can be seen that the coating consists of distinct individual layers with thicknesses of around 10nm. As the coating was being deposited, the layers have relatively smooth interfaces which conformed to the increasing roughness as the coating thickness increased.

A high-resolution image of a typical interface of coating SAg10 between the S-phase and silver layers is presented in Figure 13. Lattice fringes for both layers can be observed. The distance between the fringes for both layers are almost identical. The fringes of the S-phase layer appear blurred when compared with those of the silver layer. This is potentially due to the inconsistent expansion of the face centre cubic structure within the S-phase layer. Epitaxial growth behaviour can be observed at the interface of the two layers since the ends of the lattice fringes are interconnected, the lattice fringes are almost parallel and no foreign material is present between the layers.

Figure 14 shows the cross-sectional STEM HAADF electron image of the SAg10 multilayer coating, as well as the respective EDS chemical maps for silver, iron and nitrogen. The EDS chemical maps show that the bright layer within the electron image consists of a silver rich layer while the darker layers consist of layers rich in iron and nitrogen. These EDS maps prove that these layers consist of alternating silver and S-phase layers.

Figure 15 (a, b) depict the cross-sectional TEM BF image of the whole coating, and the respective SAD pattern for the selected area respectively. The phases identified include chromium (interfacial layer), S-phase, silver, silver oxide (Ag_2O) and silver iron oxide ($AgFeO_2$). The spots/arcs in Figure 15 (b) are labelled with the respective phase identified. The bright field image in Figure 15 (a) exhibits the presence of dark particles within the multilayer coating. Given that such image was recorded using the same specimen of Figure 12 but six months afterwards and that the SAD pattern in Figure 15 (b) highlighted the presence of oxides it is hypothesised that these particles are silver oxides which formed naturally.

3.4 Antibacterial efficacy

Figure 16 and Figure 17 show graphically the antibacterial efficacy of all monolayer and multilayer coatings respectively investigated using *Staphylococcus aureus*. The negative control results are also plotted. The positive control specimen achieved 100% reduction rate whilst the negative control specimen revealed negative bascterials reduction rate for all time periods.

All three silver containing S-phase monolayers exhibited positive bacteria reduction rate initially in Figure 16 (a). At the test duration is increased such reduction rate slows and eventually bacteria proliferates again. It can be noted that at higher silver concentrations the positive percentage reduction is maintained for a longer period of time. The copper containing S-phase monolayer in Figure 16 (b) exhibited less antibacterial efficacy against *Staphylococcus aureus*. Only coating SCuhi exhibited positive bacterial reduction rate which was only maintained up to a maximum period of 2 hours.

The multilayer coatings containing silver [Figure 17 (a)] exhibited varying antibacterial efficacy as the layer thicknesses varied. SAg2.5 exhibited the highest antibacterial efficacy across the whole range of testing period as a positive average reduction rate was maintained. SAg10 and SAg35 exhibited reduction rates similar to those of the negative control hence no antibacterial efficacy was evident. Figure 17 (b) shows that the copper multilayer SCu35 exhibited a complete bacteria elimination at a test period of 1 hour while SCu10 exhibited a near complete elimination after 2 hours of testing. The performance of SCu2.5 was similar to that of the negative control specimen as no antibacterial efficacy is shown.

4. Conclusions

- Silver and copper have been successfully co-deposited with S-phase to form monolayers in a bid to further functionalise the S-phase layer with significant anti-bacterial properties.

- CFMSIP offers significant flexibility in terms of silver/copper concentration and layer architecture.
- Ultra-saturation of the S-phase structure is possible by adding silver in a monolayer or multilayer format
- Epitaxial growth between silver and S-phase layers can significantly influence the nitrogen concentration of the S-phase layer.
- The antibacterial efficacy of the SCu10 and SCu35 coatings against *Staphylococcus Aureus* was found to be high and good for long-term self-sanitising components. However the S-phase – silver multilayers did not exhibit a 100% elimination rate as their antibacterial efficacy was significantly lower.
- Such S-phase crystal tailoring could pave the way to help understand better the structure of S-phase and how we can further functionalise such surfaces for industrial benefits.

References

[1] European Centre for Disease Prevention and Control, Surveillance of surgical site infections in Europe (2008-2009), European Centre for Disease Prevention and Control (ECDC), European Union, 2009.
[2] C. Feied, Novel antimicrobial surface coatings and the potential for reduced fomite transmission of SARS and other pathogens, DOI (2004).
[3] Surveillance of surgical site infections in Europe (2010-2011), European Centre for Disease Prevention and Control (ECDC), European Union, 2011.
[4] A.L. Bisno, F.A. Waldvogel, Infections associated with indwelling medical devices, 2nd ed., American Society for Microbiology, Washington, DC, 1994.
[5] Y. Mehta, A. Gupta, S. Todi, S.N. Myatra, D.P. Samaddar, V. Patil, P.K. Bhattacharya, S. Ramasubban, Guidelines for prevention of hospital acquired infections, Indian Journal of Critical Care Medicine : Peer-reviewed, Official Publication of Indian Society of Critical Care Medicine, 18 (2014) 149-163.
[6] J.S. Lee, W.L. Murphy, Functionalizing Calcium Phosphate Biomaterials with Antibacterial Silver Particles, Adv. Mater., 25 (2013) 1173-1179.
[7] G.A.J. Ayliffe, M.P. English, Hospital Infection: From Miasmas to MRSA, Cambridge University Press, United Kingdom, 2003.
[8] B.D. Ratner, A.S. Hoffman, F.J. Schoen, J.E. Lemons, Biomaterials Science: An Introduction to Materials in Medicine, Elsevier Academic Press, London, 2004.
[9] T. Suzuki, S.J. Morgan, W.R. Smith, P.F. Stahel, S.A. Gillani, D.J. Hak, Postoperative surgical site infection following acetabular fracture fixation, Injury, 41 (2010) 396-399.
[10] J.A. Helsen, H.J. Breme, Metals as Biomaterials John Wiley & Sons, UK, 1998.
[11] G.L. Winters, M.J. Nutt, Stainless Steels for Medical and Surgical Applications, ASTM International, Pittsbutgh, 2002.
[12] M. Godec, A. Kocijan, D. Dolinar, D. Mandrino, M. Jenko, V. Antolic, An investigation of the aseptic loosening of an AISI 316L stainless steel hip prosthesis, Biomedical materials (Bristol, England), 5 (2010) 045012.
[13] H. Dong, S-phase surface engineering of Fe-Cr, Co-Cr and Ni-Cr alloys, International Materials Reviews, 55 (2010) 65-98.
[14] D. Formosa, R. Hunger, A. Spiteri, H. Dong, E. Sinagra, J. Buhagiar, Corrosion behaviour of carbon S-phase created on Ni-free biomedical stainless steel, Surface and Coatings Technology, 206 (2012) 3479-3487.
[15] M. Sumita, T. Hanawa, S.H. Teoh, Development of nitrogen-containing nickel-free austenitic stainles ssteel for metallic biomaterials - review, Materials Science and Engineering C 24, DOI (2004) 753-760.
[16] L. Ristic, D. Vucevic, L. Radovic, S. Djordjevic, M. Nikacevic, M. Colic, Corrosive and Cytotoxic Properties of Compact Specimens and Microparticles of Ni-Cr Dental Alloy, J. Prosthodont., 23 (2014) 221-226.
[17] Y. Sun, P.A. Dearnley, Tribocorrosion Behavior of Duplex S/Cr(N) and S/Cr(C) Coatings on CoCrMo Alloy in 0.89 % NaCl Solution, J Bio Tribo Corros, 1 (2015) 1-13.
[18] K.L. Dahm, A.J. Betts, P.A. Dearnley, Chemical structure and corrosion behaviour of S phase coatings, Surface Engineering, 26 (2010) 271-276.
[19] E. Grigore, C. Ruset, X. Li, H. Dong, Synthesis and Characterization of (C, N)-Alloyed Stainless Steel Coatings by High Energy Ion Assisted Magnetron Sputtering Deposition, Materials and Manufacturing Processes, 25 (2010) 341-344.
[20] E. Grigore, C. Ruset, X. Li, H. Dong, Comparison of Magnetron Deposited N-Alloyed Stainless Steel Coatings and Low Temperature Plasma Nitrided Austenitic Stainless Steel, Plasma Processes and Polymers, 6 (2009) S321-S325.
[21] Y. Dong, X. Li, L. Tian, R.L. Sammons, H. Dong, Towards long-lasting antibacterial stainless steel surfaces by combining double glow plasma silvering with active screen plasma nitriding, Acta Biomaterialia, DOI (2011) 447-457.

[22] Y. Dong, X. Li, R. Sammons, H. Dong, The Generation of Wear-Resistant Antimicrobial Stainless Steel Surfaces by Active Screen Plasma Alloying with N and Nanocrystalline Ag, Journal of Biomedical Materials Research Part B-Applied Biomaterials, 93B (2010) 185-193.
[23] Y.Z. Wan, S. Raman, F. He, Y. Huang, Surface modification of medical metals by ion implantation of silver and copper, Vacuum, 81 (2007) 1114-1118.
[24] B. Khodashenas, The Influential Factors on Antibacterial Behaviour of Copper and Silver Nanoparticles, Indian Chemical Engineer, 58 (2016) 224-239.
[25] JIS, JIS Z 2801:2000 - Antimicrobial products-Test for antimicrobial activity and efficacy, Japanese Industrial Standard, 1993.
[26] B.E. ISO, 22196 - Measurement of antibacterial activity on plastics and other non-porous surfaces, BSI Standards, 2011.
[27] K.L. Dahm, P.A. Dearnley, S-phase coatings by unbalanced magnetron sputtering, Minerals, Metals & Materials Soc, Warrendale, 1996.
[28] C.G.F. Pina, P.A. Dearnley, J. Fisher, UHMWPE wear response to apposing nitrogen S-phase coated and uncoated orthopaedic implant grade stainless steel, Wear, 267 (2009) 743-752.
[29] C.G.F. Pina, K.L. Dahm, J. Fisher, P.A. Dearnley, Characteristics and corrosion-wear response of S-phase coated ortron 90, 2004.
[30] K.L. Dahm, P.A. Dearnley, On the nature, properties and wear response of S-phase (nitrogen-alloyed stainless steel) coatings on AISI 316L, Proc. Inst. Mech. Eng. Pt. L-J. Mater.-Design Appl., 214 (2000) 181-198.
[31] S.C. Gallo, H. Dong, On the fundamental mechanisms of active screen plasma nitriding, Vacuum, 84 (2009) 321-325.

List of figure captions

- Figure 17 - Antibacterial efficacy of the (a) silver, (b) copper containing S-phase multilayer coatings and the negative control at different length of experimentation with Staphylococcus aureus bacteria.

Figures

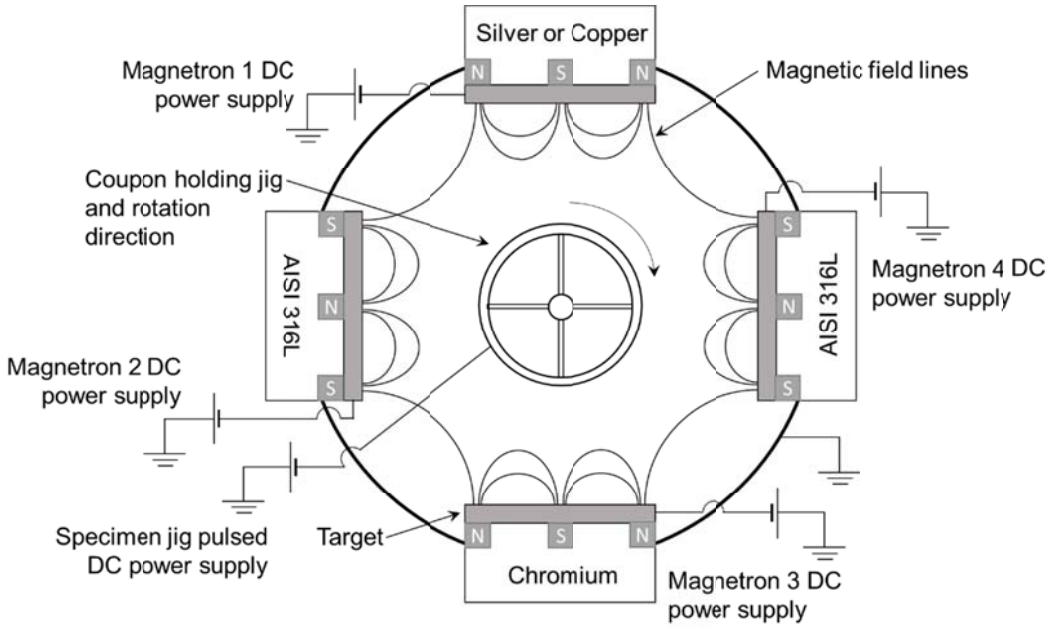

Figure 1

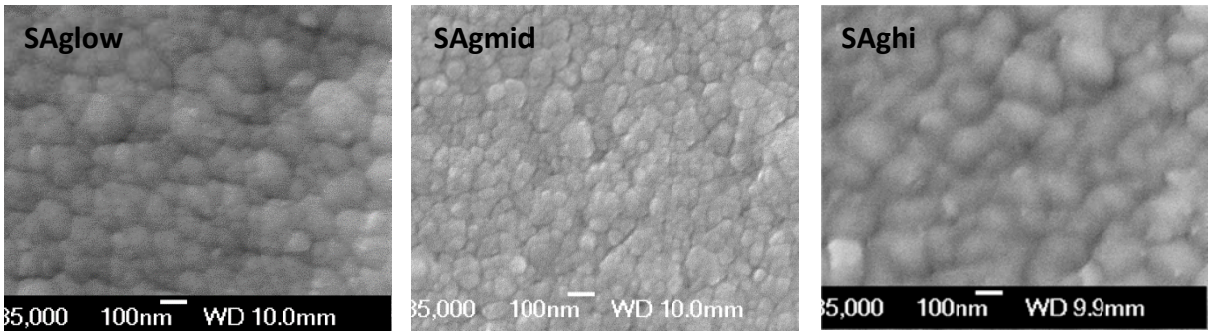

(a)

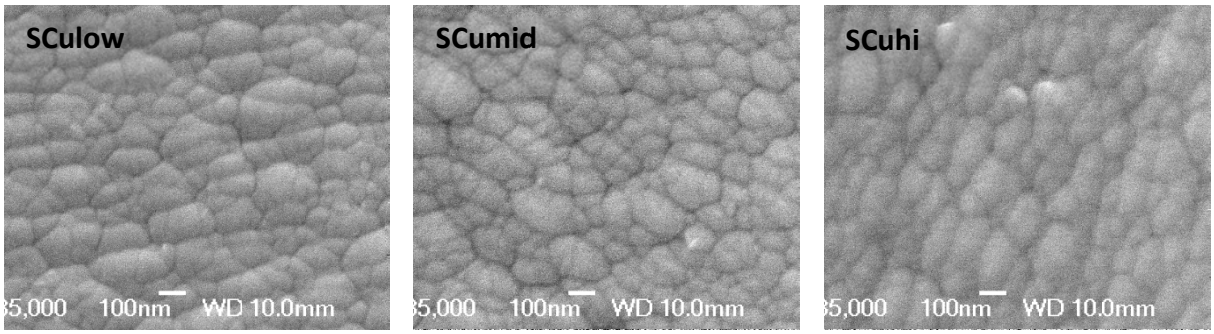

(b)

Figure 2

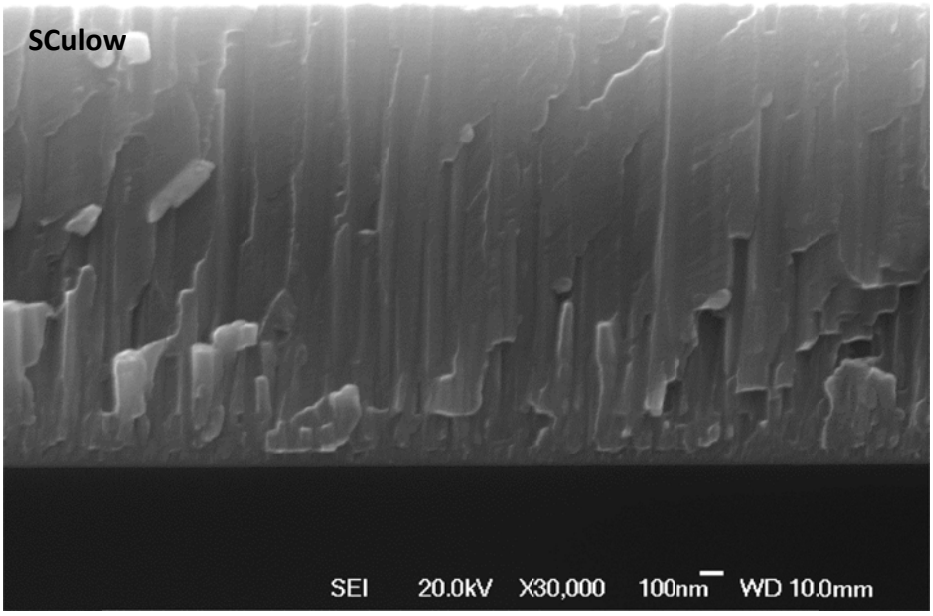

Figure 3

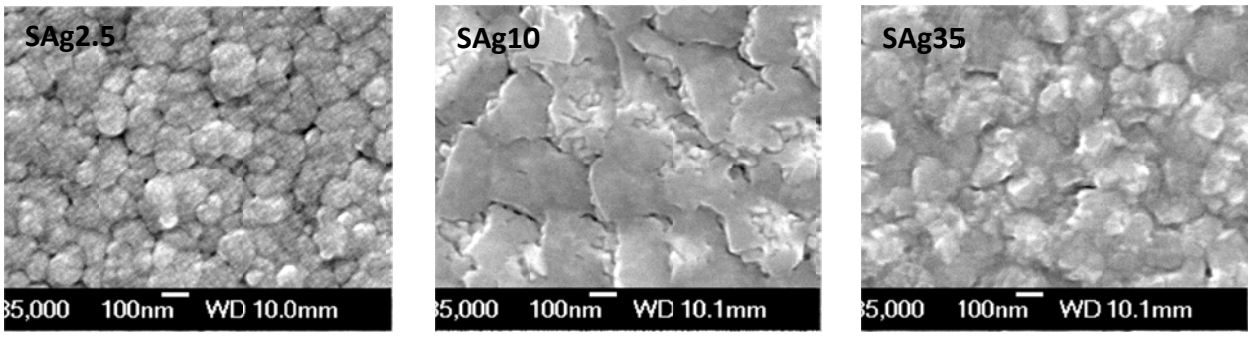

(a)

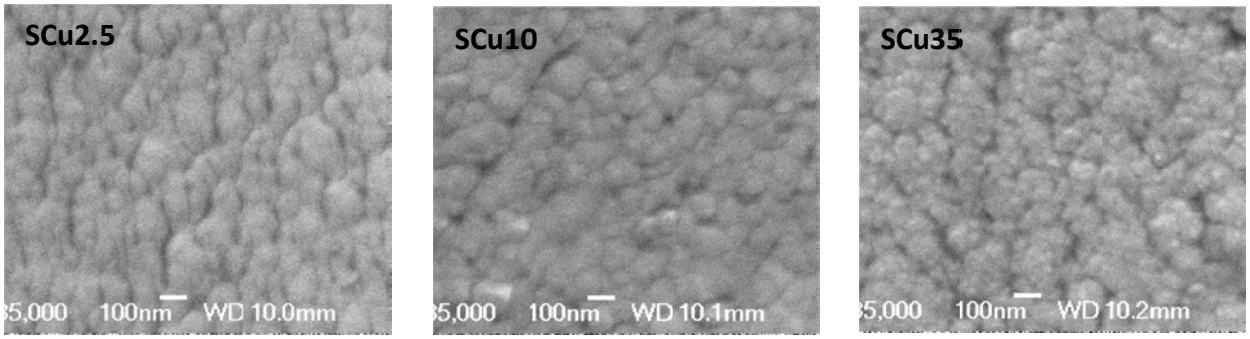

(b)

Figure 4

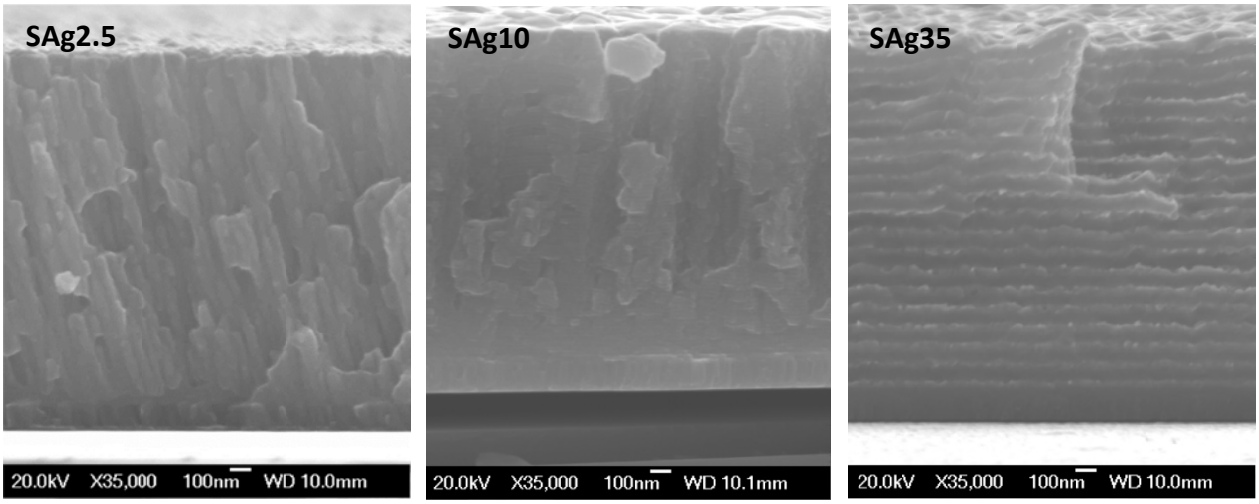

Figure 5

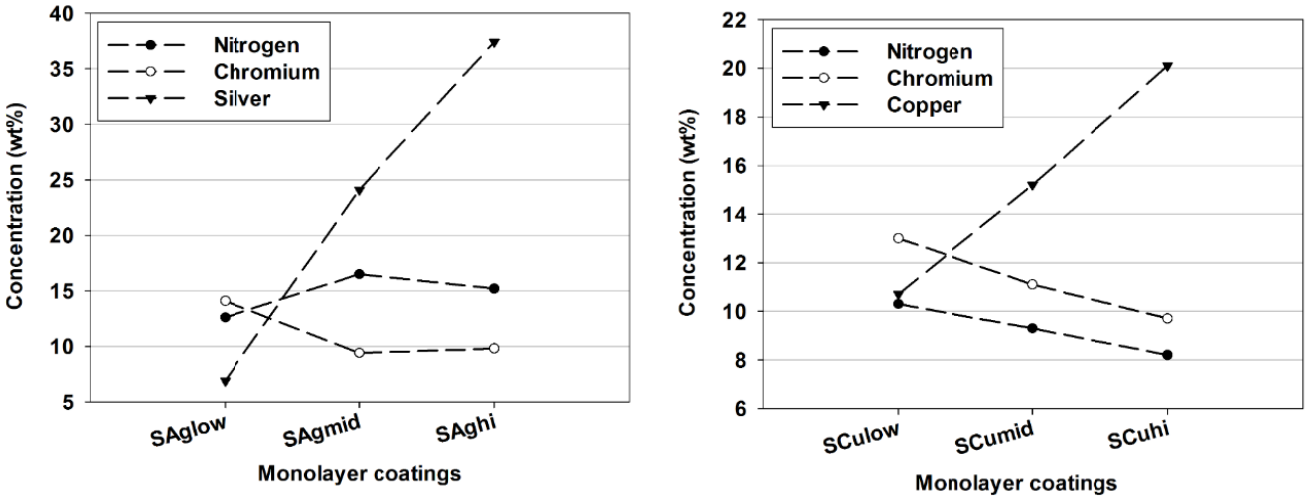

(a) (b)

Figure 6

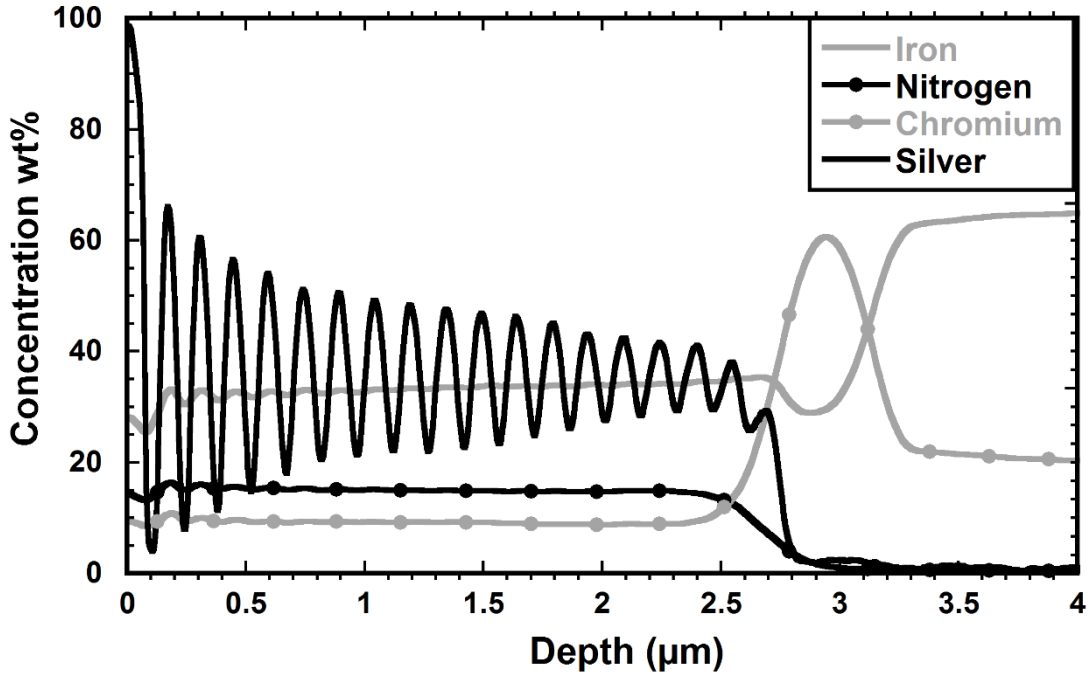
Concentration wt%
Depth (μm)
Iron
Nitrogen
Chromium
Silver
0
20
40
60
80
100
0
0.5
1
1.5
2
2.5
3
3.5
4

Figure 7

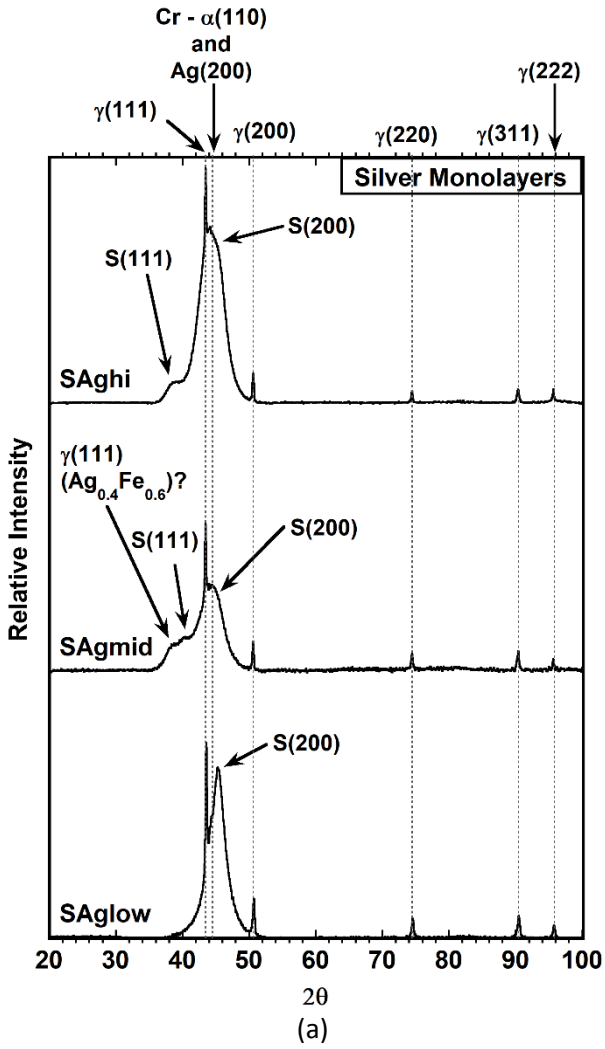
Cr - α(110)
and
Ag(200)
γ(111)
γ(200)
γ(220)
γ(311)
γ(222)
Silver Monolayers
S(111)
S(200)
SAghi
γ(111)
(Ag0.4Fe0.6)?
S(111)
S(200)
SAgmid
S(200)
SAglow
Relative Intensity
20 30 40 50 60 70 80 90 100
2θ
(a)

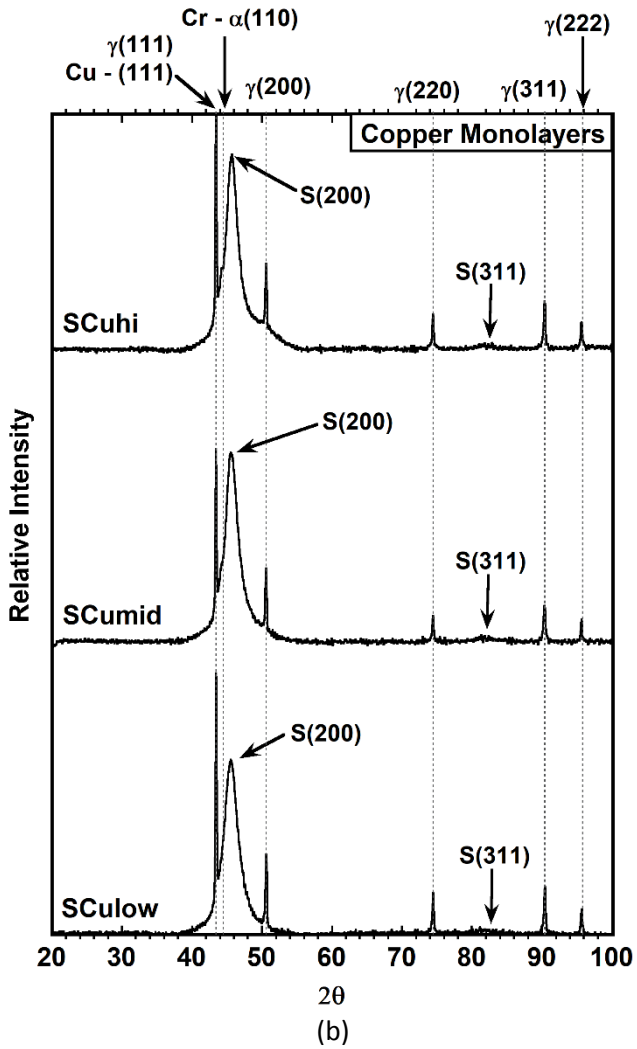
Cr - α(110)
γ(111)
Cu - (111)
γ(200)
γ(220)
γ(311)
γ(222)
Copper Monolayers
S(200)
S(311)
SCuhi
S(200)
S(311)
SCumid
S(200)
S(311)
SCulow
Relative Intensity
20 30 40 50 60 70 80 90 100
2θ
(b)

Figure 8

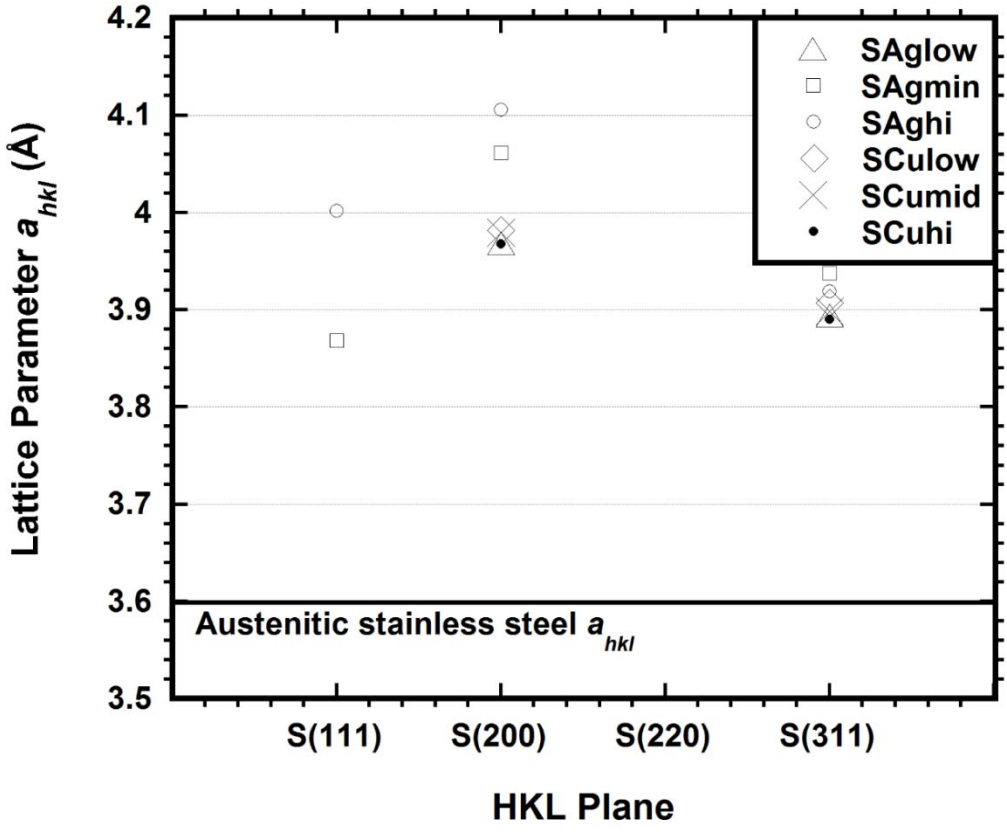
4.2
4.1
4
3.9
3.8
3.7
3.6
3.5
Lattice Parameter a_{hkl} (Å)
SAglow
SAgmin
SAghi
SCulow
SCumid
SCuhi
Austenitic stainless steel a_{hkl}
S(111)
S(200)
S(220)
S(311)
HKL Plane

Figure 9

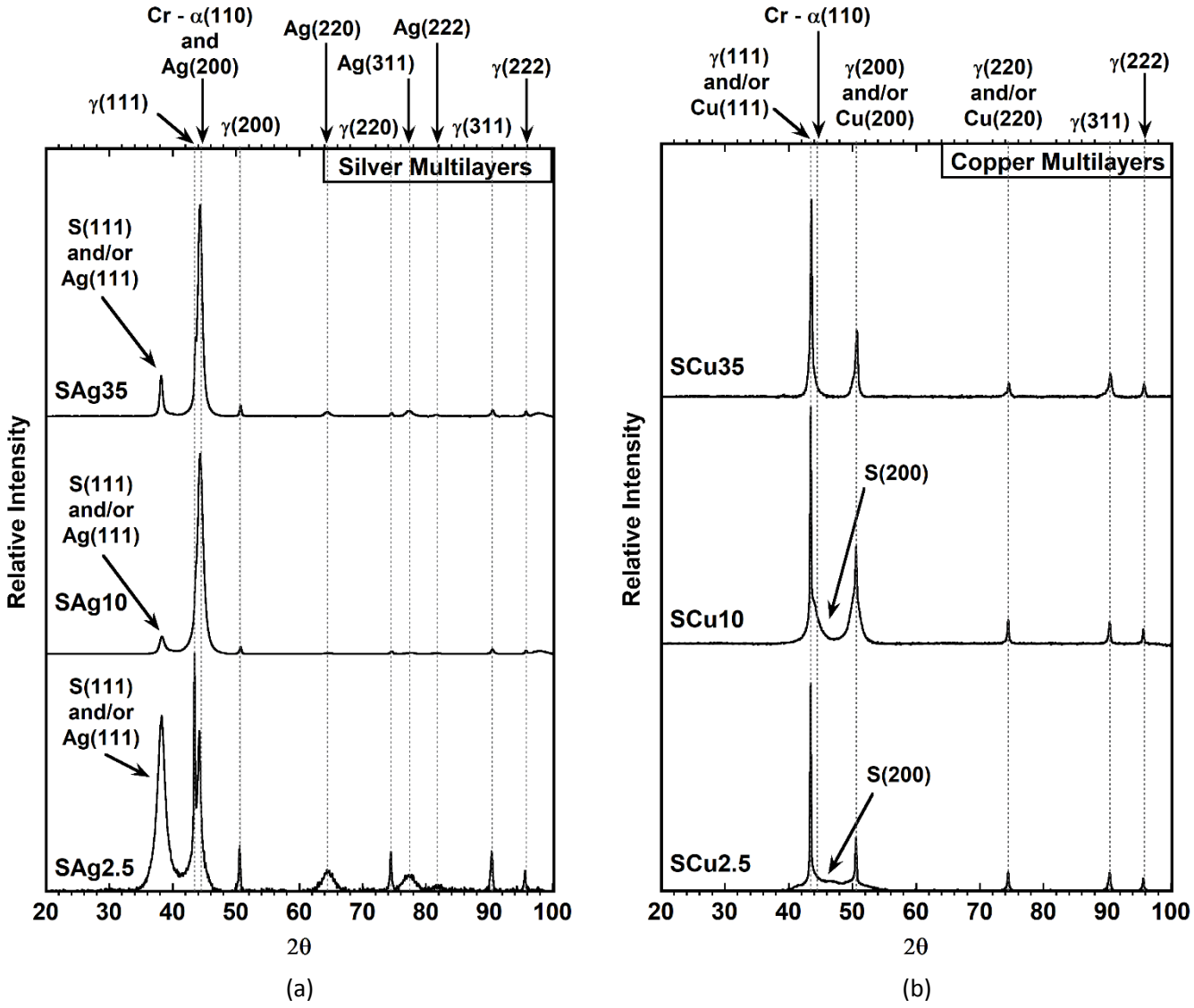
Cr - α(110)
and
Ag(200)
Ag(220)
Ag(222)
Ag(311)
γ(222)
γ(111)
γ(200)
γ(220)
γ(311)
Silver Multilayers
S(111)
and/or
Ag(111)
SAg35
S(111)
and/or
Ag(111)
SAg10
S(111)
and/or
Ag(111)
SAg2.5
Relative Intensity
20 30 40 50 60 70 80 90 100
2θ
(a)
Cr - α(110)
γ(111)
and/or
Cu(111)
γ(200)
and/or
Cu(200)
γ(220)
and/or
Cu(220)
γ(311)
γ(222)
Copper Multilayers
SCu35
S(200)
SCu10
S(200)
SCu2.5
Relative Intensity
20 30 40 50 60 70 80 90 100
2θ
(b)

Figure 10

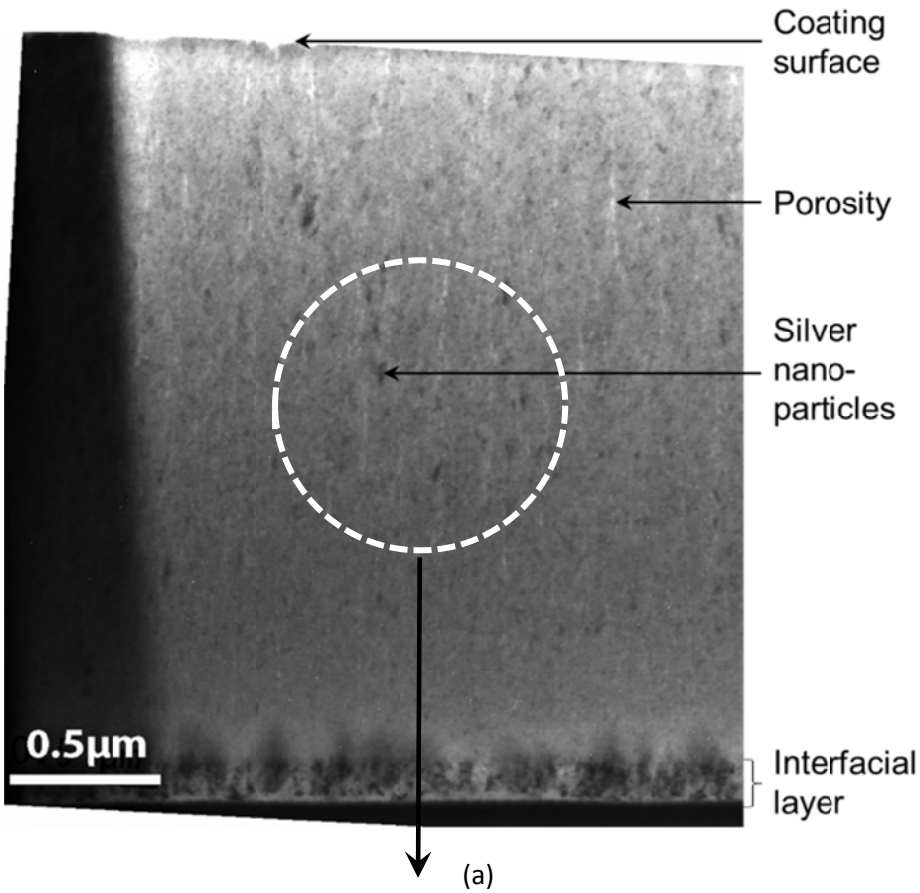
Coating surface
Porosity
Silver nano-particles
0.5µm
Interfacial layer

(a)

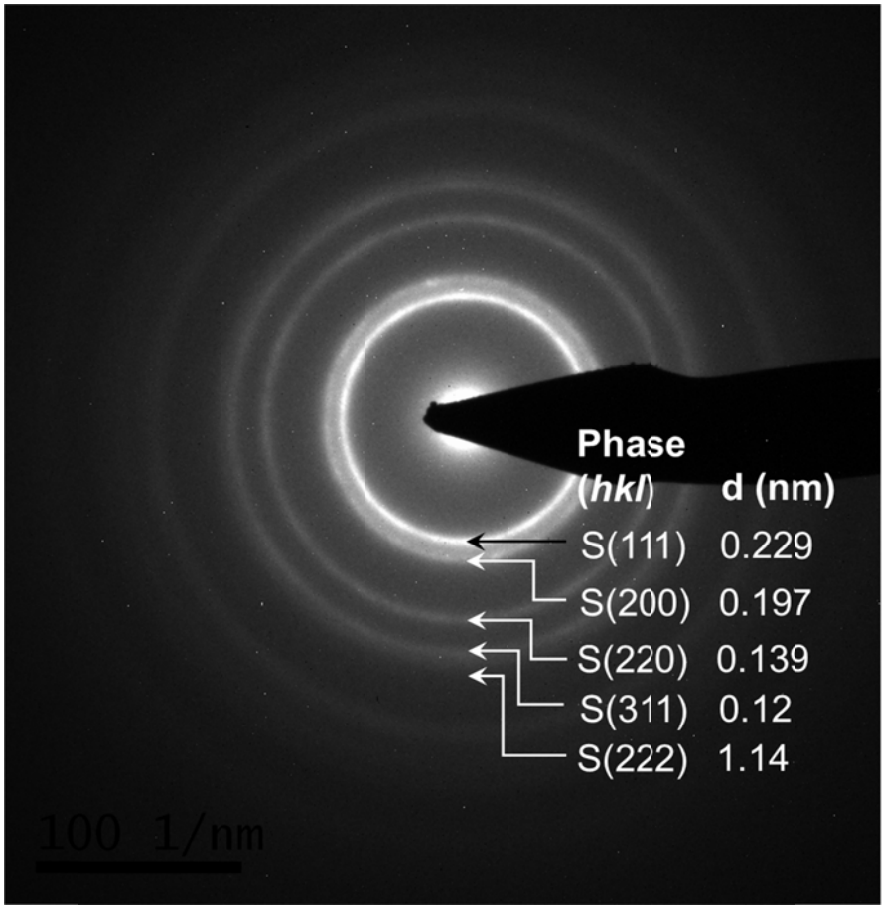
Phase (hkl) d (nm)
S(111) 0.229
S(200) 0.197
S(220) 0.139
S(311) 0.12
S(222) 1.14
100 1/nm

(b)

Figure 11

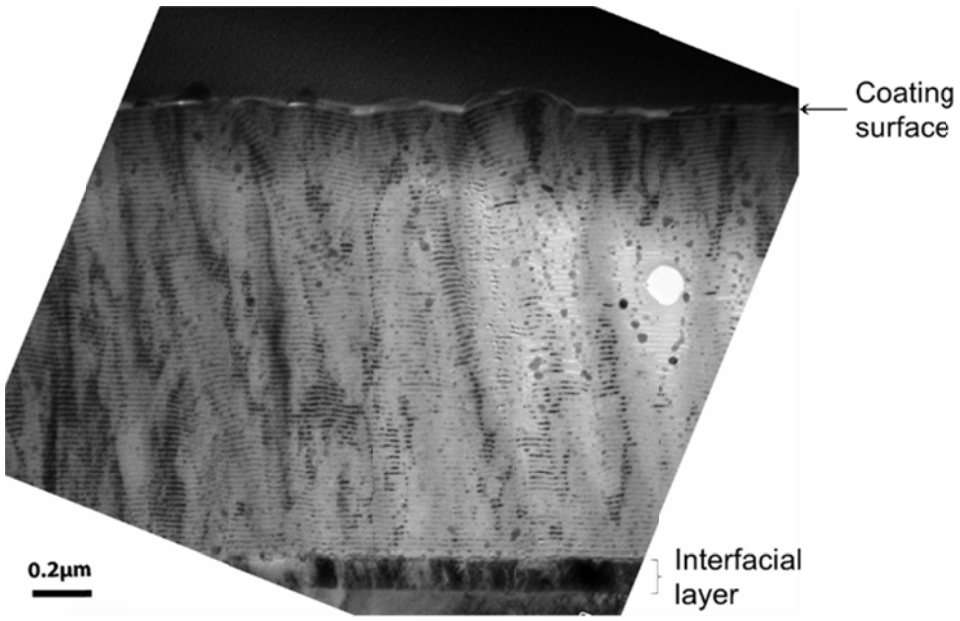
Coating
surface
0.2µm
Interfacial
layer

(a)

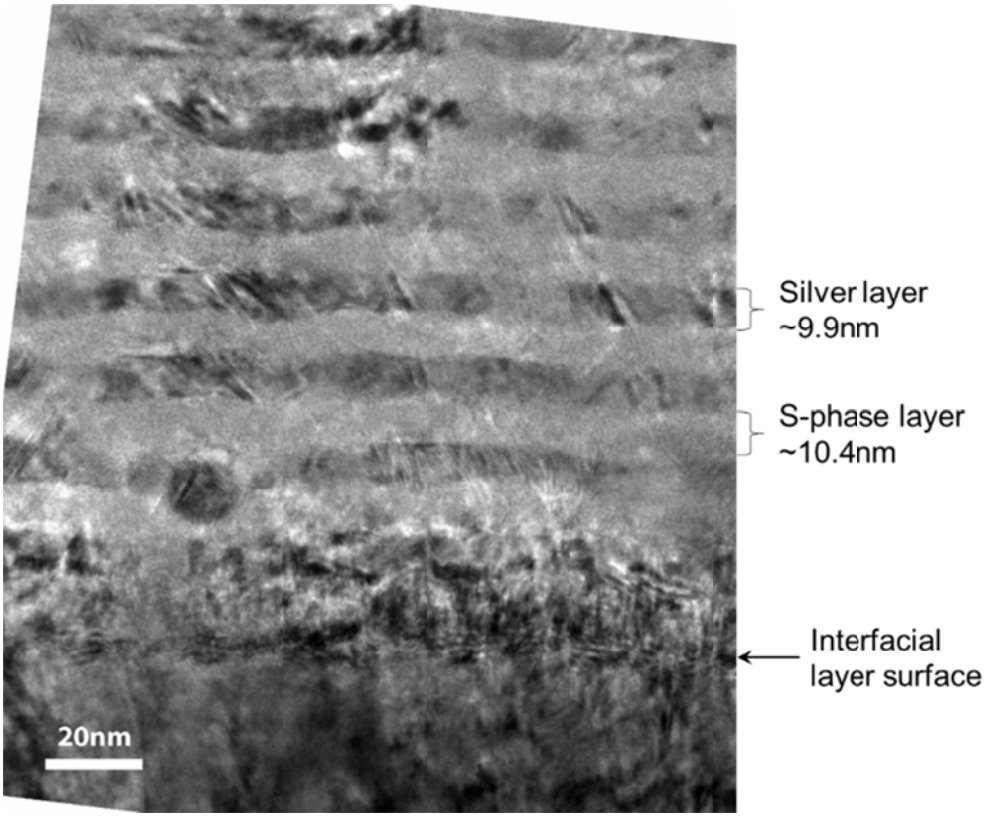
Silver layer
~9.9nm
S-phase layer
~10.4nm
Interfacial
layer surface
20nm

(b)

Figure 12

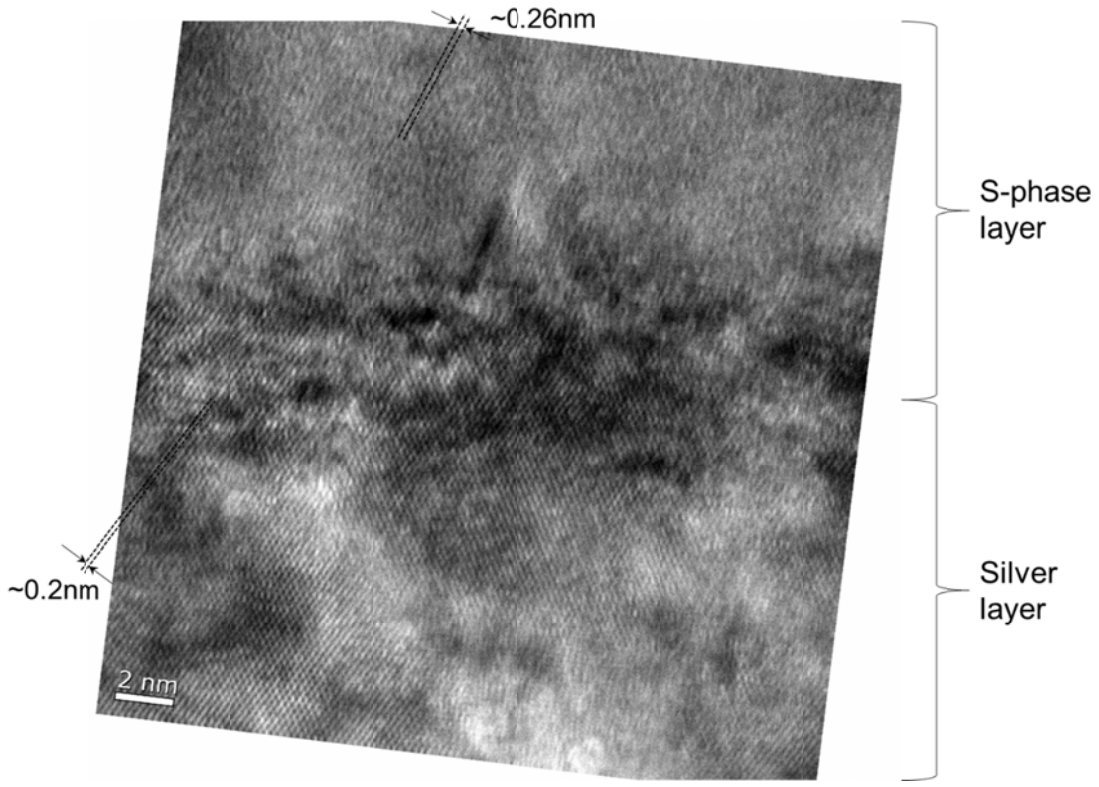

Figure 13

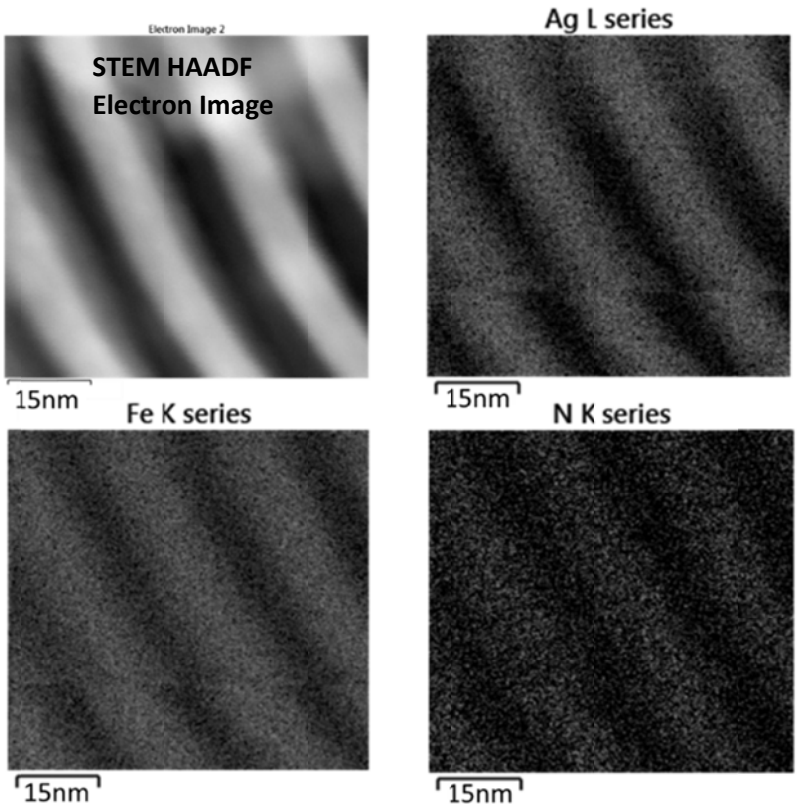
Electron Image 2
STEM HAADF
Electron Image
15nm
Ag L series
15nm
Fe K series
15nm
N K series
15nm

Figure 14

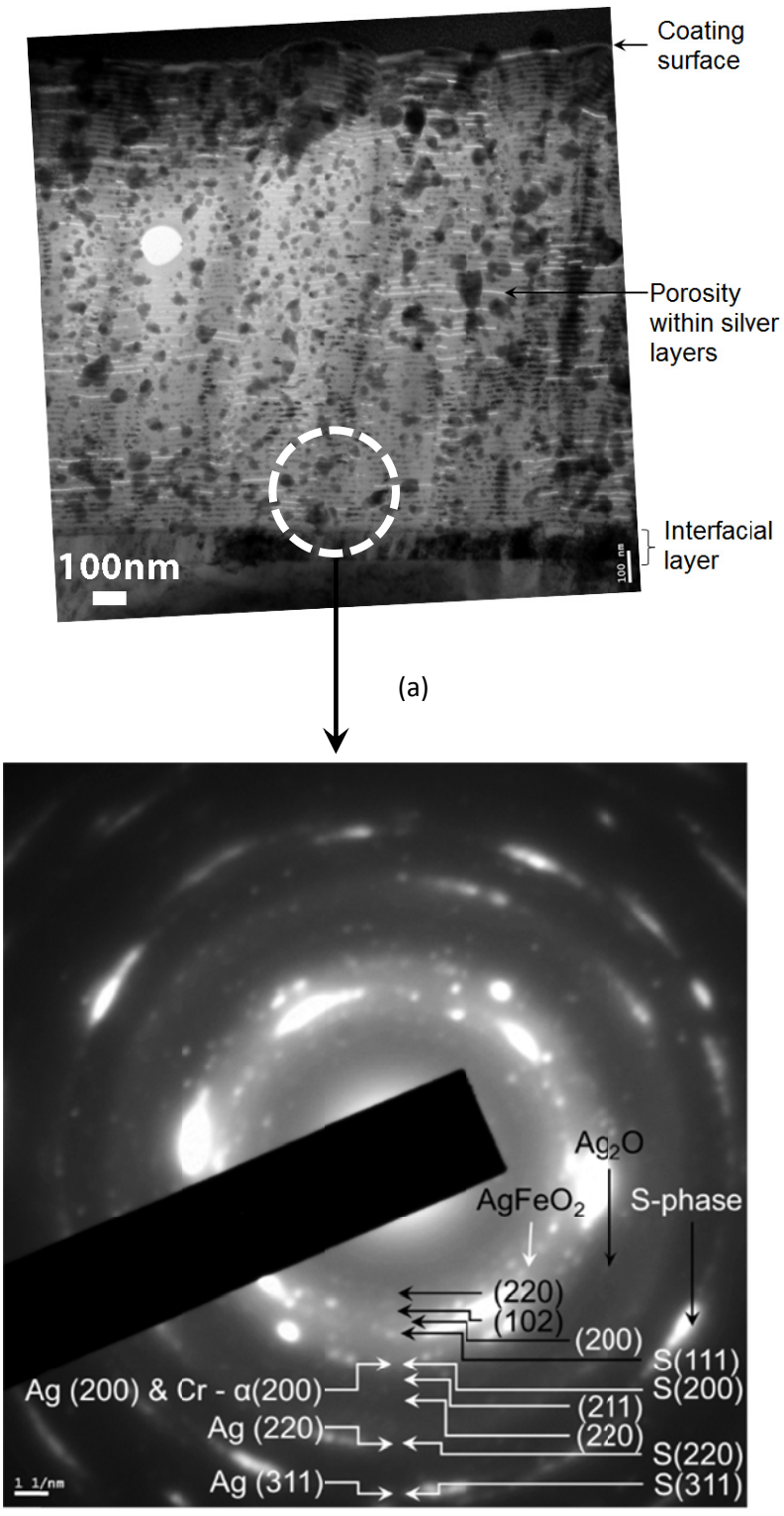
Coating surface
Porosity within silver layers
Interfacial layer
100nm
100 nm
(a)
Ag2O
AgFeO2
S-phase
(220)
(102)
(200)
S(111)
S(200)
Ag (200) & Cr - α(200)
(211)
Ag (220)
(220)
S(220)
Ag (311)
S(311)
1 1/nm
(b)

Figure 15

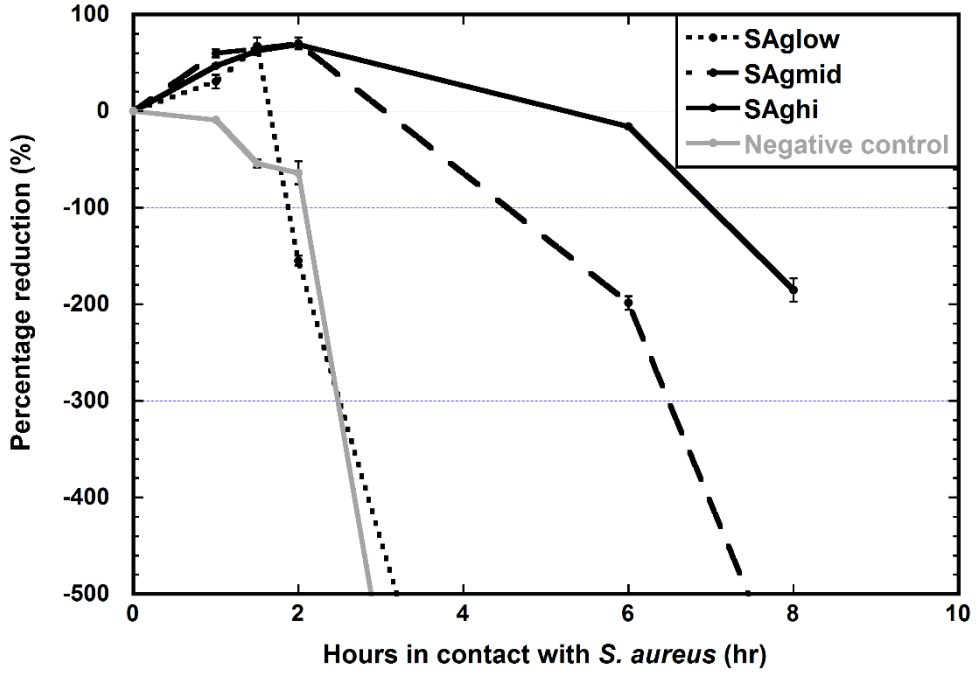
100
0
-100
-200
-300
-400
-500
Percentage reduction (%)
0
2
4
6
8
10
Hours in contact with S. aureus (hr)
SAglow
SAgmid
SAghi
Negative control

(a)

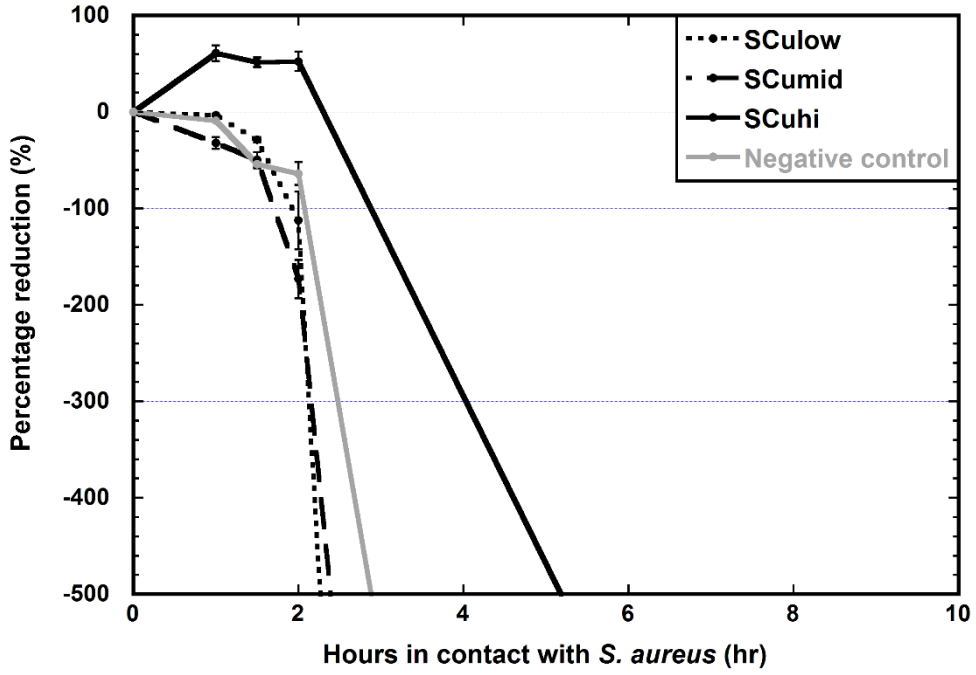
100
0
-100
-200
-300
-400
-500
Percentage reduction (%)
0
2
4
6
8
10
Hours in contact with S. aureus (hr)
SCulow
SCumid
SCuhi
Negative control

(b)

Figure 16

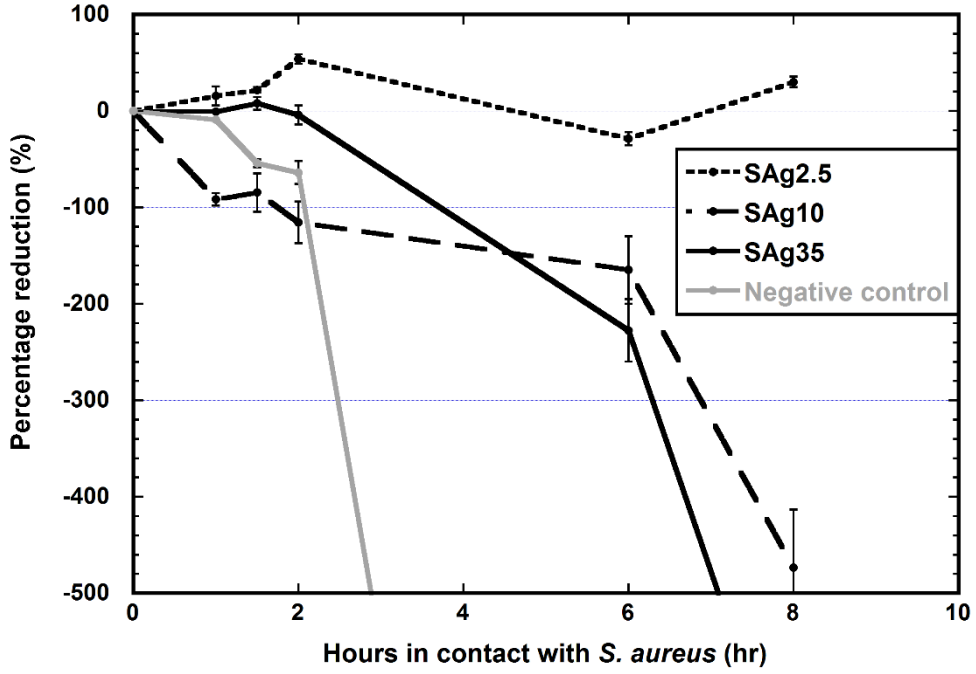
100
0
-100
-200
-300
-400
-500
Percentage reduction (%)
0
2
4
6
8
10
Hours in contact with S. aureus (hr)
SAg2.5
SAg10
SAg35
Negative control

(a)

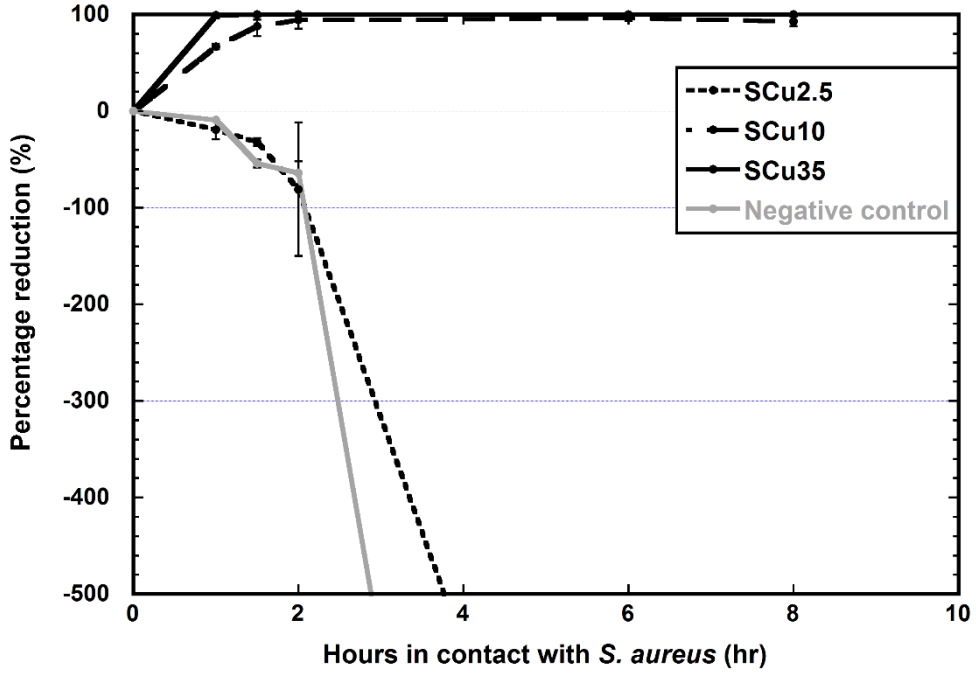
100
0
-100
-200
-300
-400
-500
Percentage reduction (%)
0
2
4
6
8
10
Hours in contact with S. aureus (hr)
SCu2.5
SCu10
SCu35
Negative control

(b)

Figure 17